Systematic study of the pp → ppω reaction

The COSY-TOF Collaboration

M. Abdel-Bary[3], S. Abdel-Samad[3], K.-Th. Brinkmann[1], H. Clement[4], J. Dietrich[1], E. Doroshkevich[4], S. Dshemuchadse[1], K. Ehrhardt[4], A. Erhardt[4], W. Eyrich[2], A. Filippi[7], H. Freiesleben[1], M. Fritsch[2], W. Gast[3], A. Gillitzer[3], J. Gottwald[1], H. Jäger[3], B. Jakob[1], R. Jäkel[1], L. Karsch[1], K. Kilian[3], H. Koch[8], M. Krapp[2], J. Kreß[4], E. Kuhlmann[1], A. Lehmann[2], S. Marcello[7], S. Mauro[8], P. Michel[5], K. Möller[5], H. P. Morsch[3,6], L. Naumann[5], N. Paul[3], C. Pizzolotto[2], Ch. Plettner[1], S. Reimann[1], M. Richter[1], J. Ritman[3], E. Roderburg[3], A. Schamlott[5], P. Schönmeier[1], W. Schroeder[2], M. Schulte-Wissermann[1], T. Sefzick[3], M. Steinke[8], G. Y. Sun[1], A. Teufel[2], W. Ullrich[1], G. J. Wagner[4], M. Wagner[2], R. Wenzel[1], A. Wilms[8], P. Wintz[3], P. Wüstner[3], and P. Zupranski[6]

[1] Institut für Kern- und Teilchenphysik, Technische Universität Dresden, D-01062 Dresden, Germany
[2] Physikalisches Institut, Universität Erlangen-Nürnberg, D-91058 Erlangen, Germany
[3] Institut für Kernphysik, Forschungszentrum Jülich, D-52425 Jülich, Germany
[4] Physikalisches Institut, Universität Tübingen, D-72076 Tübingen, Germany
[5] Institut für Kern- und Hadronenphysik, Forschungszentrum Dresden-Rossendorf, D-01314 Dresden, Germany
[6] Soltan Institute for Nuclear Studies, 05-400 Swierk/Otwock, Poland
[7] INFN Torino, 10125 Torino, Italy
[8] Institut für Experimentalphysik, Ruhr-Universität Bochum, D-44780 Bochum, Germany

Abstract. A systematic study of the production of ω-mesons in proton-proton-collisions was carried out in a kinematically complete experiment at three excess energies ($\varepsilon = 92, 128, 173$ MeV). Both protons were detected using the large-acceptance COSY-TOF spectrometer at an external beam line at the Cooler Synchrotron COSY at Forschungszentrum Jülich. The total cross section, angular distributions of both ω-mesons and protons were measured and presented in various reference frames such as the overall CMS, helicity and Jackson frame. In addition, the orientation of the ω-spin and invariant mass spectra were determined. We observe ω-production to take place dominantly in Ss and Sp final states at $\varepsilon = 92, 128$ MeV and, additionally, in Sd at $\varepsilon = 173$ MeV. No obvious indication of resonant ω-production via N^*-resonances was found, as proton angular distributions are almost isotropic and invariant mass spectra are compatible with phase space distributions. A dominant role of $^3P_1$ and $^1S_0$ initial partial waves for ω-production was concluded from the orientation of the decay plane of the ω-meson. Although the Jackson angle distributions in the ωp-Jackson frame are anisotropic we argue that this is not an indication of a resonance but rather a kinematical effect reflecting the anisotropy of the ω angular distribution. The helicity angle distribution in the ωp-helicity frame shows an anisotropy which probably reflects effects of the ω angular momenta in the final state; this observable may be, in addition to the orientation of the ω decay plane, the most sensitive one to judge the validity of theoretical descriptions of the production process.
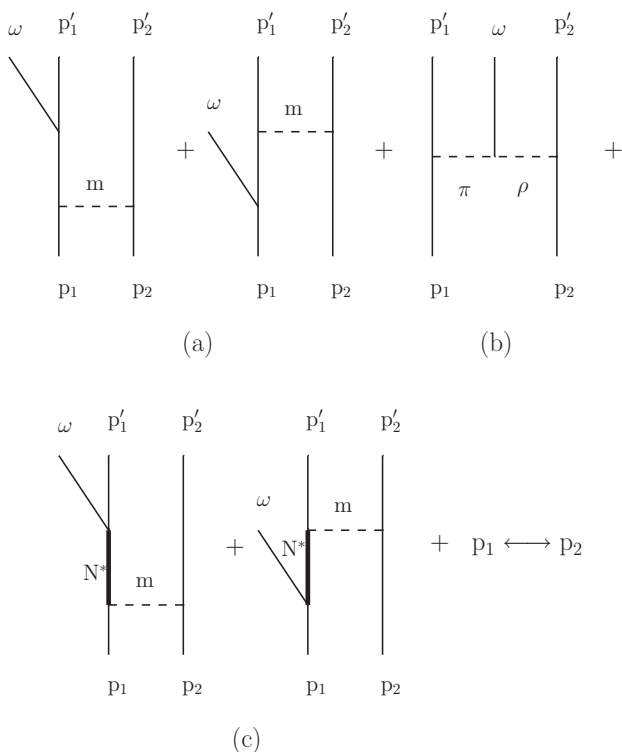
PACS. 13.75Cs Nucleon-nucleon interactions – 13.88e+ Polarization in interactions and scattering – 14.40Cs Other mesons with S=C=0, mass < 2.5 GeV – 25.10+s Nuclear reactions involving few-nucleon systems – 25.40Ve Other reactions above meson production thresholds (energies > 400 MeV)

1 Introduction

The production of ω-mesons in proton-proton collisions has come into the focus of experimental and theoretical studies only in recent years. Early measurements of production cross sections employed hydrogen bubble chambers, a compilation of those data was published by Flaminio

Correspondence to: w.ullrich@physik.tu-dresden.de (W. Ullrich)

et al. [1] for beam momenta of $p_{\text{beam}} = 3.99$ to 19.0 GeV/c. In the last 10 years several experiments have been performed with electronic detectors, namely by the DISTO collaboration at $p_{\text{beam}} = 3.67$ GeV/c [2], [3] and at beam momenta below 3.2 GeV/c by Hibou *et al.* [4], Barsov *et al.* [5], and the COSY-TOF collaboration [6], [7]. These experimental data provide, in principle, important information about the short range part of the nucleon-nucleon interaction which is dominated by the exchange of the
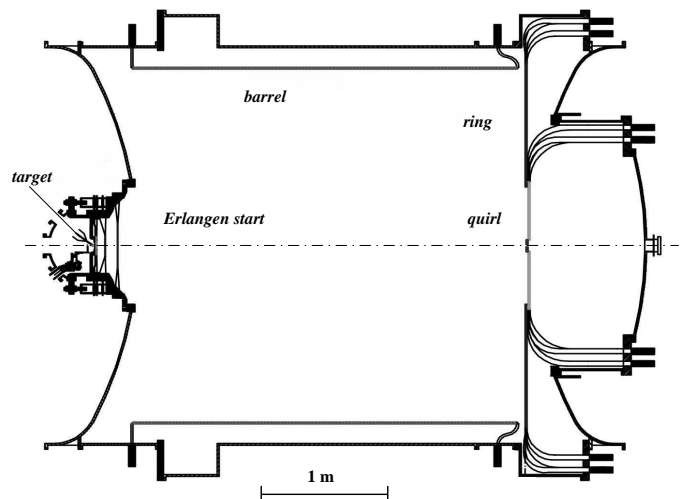
Fig. 1. Tree level diagrams for the reaction pp → ppω. Emission from (a) nucleon line, (b) internal meson line, and (c) N^*-resonance. Initial and final state interaction is not indicated.

Fig. 2. Sketch of the COSY-TOF spectrometer with its main components; see text for details.

isoscalar ω-meson [8]. They also furnish elementary cross sections needed for studies of in-medium properties of mesons.

Various theoretical models were developed to describe the experimental data. Sibirtsev [9] has investigated the ρ, ω, and ϕ-production within a one-pion exchange model. Nakayama et al. [10] described the ω-production within a meson exchange model taking into account nucleonic and meson-exchange currents. These studies were extended in [11] and [12]. The ω-production via nucleon resonances was studied by Fuchs et al. [13] and Faessler et al. [14]. Studies which include both resonant production and meson currents were performed by Kämpfer et al. [15] and Titov et al. [16]. The diagrams considered so far in theoretical calculations are shown in fig. 1.

These models were particularly tailored to reproduce the total cross sections and/or angular distributions of the ω-meson. The rather limited experimental data basis does not suffice to prove one or the other model preferable. In addition, none of the theoretical models takes into account all diagrams of fig. 1 and most of them neglect either initial or final state interactions or both.

In this paper we present a wealth of experimental data for the pp → ppω reaction obtained at three different beam momenta, namely $p_{\text{beam}} = 2.950, 3.059, 3.200 \, \text{GeV/c}$, which correspond to excess energies ($\varepsilon = \sqrt{s} - 2m_p - m_\omega$) of 92, 128, and 173 MeV, respectively. All data were taken with a special downscaled trigger in parallel to studies of

associated strangeness procuction. First evaluations of the data at 2.950 and 3.200 GeV/c, taken in 2000, focused on the angular distributions and total cross section for ω-mesons [6]. Here we show data where the method of analysis was improved and extended to other observables. The data at 3.059 GeV/c were collected in an experiment carried out with a very large integrated luminosity in 2004 as it was devoted to the search for a supposed pentaquark state [17]. Other publications of our collaboration were concerned with the measurement of the analysing power in the same reaction channel using a polarised proton beam at 3.065 GeV/c [18] and a preferred orientation of the ω decay plane [19].

This paper is organised as follows: The experimental procedure is detailed in sect. 2, describing the detector setup, the principle of measurement and data analysis, Monte Carlo simulations, and a discussion of systematic uncertainties. In sect. 3 we present and discuss the experimental results obtained for the total cross sections, angular distributions of the ω-mesons and protons in the overall centre-of-mass system (CMS), the orientation of the ω decay plane, invariant mass spectra, and distributions of both helicity and Jackson angle in their respective frames. These results set important benchmarks for any theoretical model. The paper ends with a summary.

2 Experimental procedure

2.1 Detector setup

The experiments were carried out with the time-of-flight spectrometer COSY-TOF installed at an external beam line of the COoler SYnchrotron COSY at Forschungszentrum Jülich. A sketch of the detector is shown in fig. 2.

The extracted proton beam (spill length ≈ 5 min, several 10^6 protons/s) is directed onto a liquid hydrogen target of 6 mm diameter and 4 mm length [20] through an-
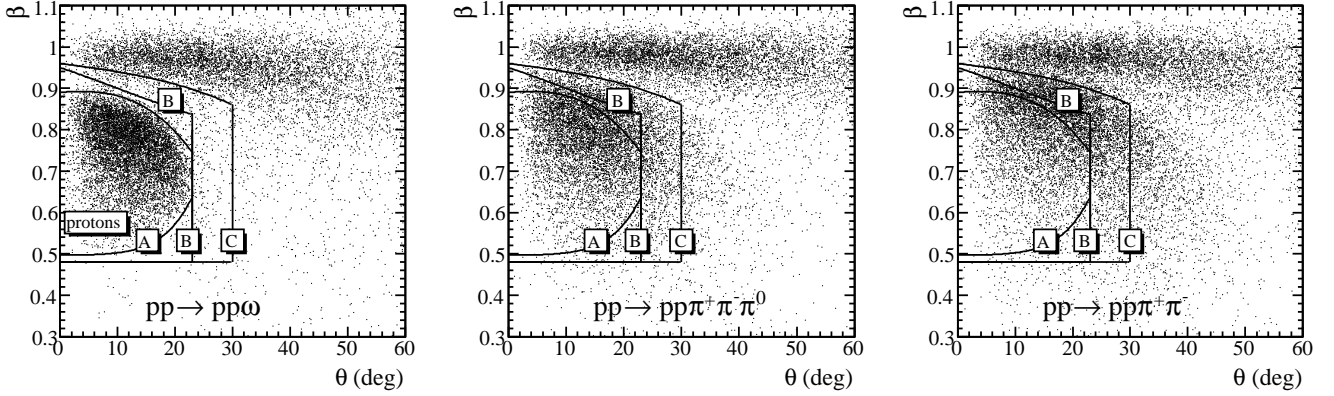
Fig. 3. Monte Carlo data for pp→ppω ($\omega \to \pi^+\pi^-\pi^0$), pp→pp$\pi^+\pi^-\pi^0$ and pp→pp$\pi^+\pi^-$ at $\varepsilon = 128$ MeV. The experimental resolution of the detector has been accounted for. Three regions (A, B, C) for the separation of protons and pions are indicated. See text for details.

nular veto detectors of different diameter positioned at 260, 51 and 3.5 cm upstream of the target. The emerging particles traverse a layered system of time-of-flight start and tracking detectors (called Erlangen start [21]). After a flight path of ≈ 3 m through the evacuated tank (0.2 Pa) all charged particles are detected in the highly granular stop components of the spectrometer. They consist of two three-layered forward hodoscopes (quirl, ring) which are built according to the layout described in [22], and a barrel hodoscope [23], all utilising BC412 scintillating material.

From the combined measurement of time and position the velocity vectors of all charged particles are determined with a time-of-flight resolution of better than $\sigma_{TOF} = 300$ ps and an angular track-resolution of better than $\sigma_\triangleleft = 0.3°$. Due to the low mass area density of the time-of-flight start and tracking detectors, the influence of small angle scattering and energy loss is almost negligible for particles with $\beta > 0.5$. Only particles with these velocities are produced in the reaction under study.

Unlike magnetic spectrometers, which often provide particle identification at the cost of limited acceptance, the COSY-TOF spectrometer stands out for its large geometrical acceptance ($1° < \theta_{lab} < 60°$, $0° < \phi < 360°$) and an efficiency $> 95\%$ for the detection of a charged particle. This allows the almost unambiguous and simultaneous identification of different reaction channels (e.g., pp→ pp, dπ^+, pp$\pi^+\pi^-$, ppω, pK$^+\Lambda$, pK$^+\Sigma^0$, pK$^0\Sigma^+$) by exploiting the time of flight of all emerging charged particles as well as the event's topology.

2.2 Principle of measurement and data analysis

The reaction pp → ppω with the main decay channel of the ω-meson ($\omega \to \pi^+\pi^-\pi^0, \mathcal{BR} \approx 89.2\%$ [24]) is preselected during data taking via a trigger set on four charged particles detected in the stop components (quirl, ring, barrel). The outgoing protons and the charged pions are, due to their large mass difference, clearly separated in a veloc-

ity versus polar angle representation as can be seen from the left frame of fig. 3; cf. also [7].

This kinematical separation serves to identify protons as they are restricted to a region with $\theta < 23°$ and moderate velocities, while the pions mainly cluster at $\beta \approx 1$ over the full angular range. There is only a small number of events (about 10 to 15% depending on excess energy) where pions are found in the proton region. For the analysis we require exactly two particles within one of the indicated proton regions A, B, or C, shown in the left frame of fig. 3 (the effect of these different regions will be discussed below), and exactly two particles outside, which are, in turn, assumed to be pions. In addition, all tracks must fall into the region of optimum geometrical acceptance ($3° < \theta < 60°$). Proton and pion masses are then assigned accordingly and the four-momenta of protons are calculated using the measured velocity vectors. Monte Carlo simulations showed that the assignment of protons and pions to the pp→ppω reaction channel based on these criteria is correct for 99.2% of all events. We would like to point out that the geometrical acceptance for pp → ppω → pp$\pi^+\pi^-\pi^0$ reactions, that means the fraction of events with all 4 charged particles in the geometrical covered region, is 65% at the lower excess energy $\varepsilon = 92$MeV and increases to 68% at $\varepsilon = 173$MeV. This applies for phase space and isotropic distributed events.

The missing mass distribution calculated from the momenta of the identified protons exhibits a peak at the ω-mass. However, this spectrum contains a large contribution of resonant two pion production via pp→ ppρ, $\rho \to \pi^+\pi^-$ and non-resonant production of two pions (pp → pp$\pi^+\pi^-$) as well as three pions (pp→pp$\pi^+\pi^-\pi^0$), all of them constituting the major components of an unavoidable physical background. In order to accentuate this point, we show in the middle (right hand) frame of fig. 3 Monte-Carlo simulated data for non-resonant $\pi^+\pi^-\pi^0$ ($\pi^+\pi^-$) production. It is obvious that in these two cases the kinematical separation of protons and pions is less certain.

It is possible to reduce the two-pion background by exploiting the topology of the ω-decay into three pions.
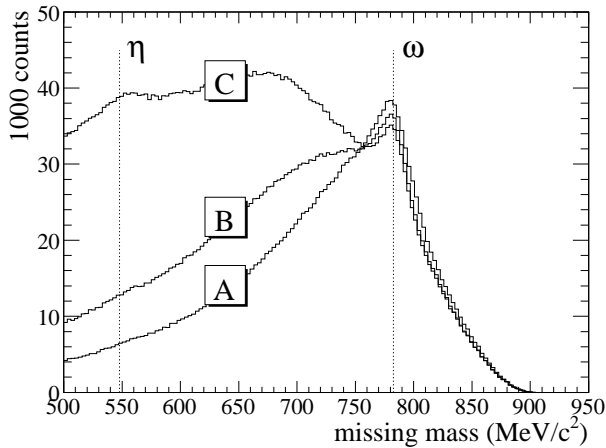
Fig. 4. Proton-proton missing mass spectra at $\varepsilon = 128\,\mathrm{MeV}$ obtained when applying the different regions for proton assignment shown in fig. 3.

Here, the plane defined by the two charged pions does, in general, not contain the pp-missing momentum vector ($= \omega$-momentum vector) due to the momentum of the undetected π^0. By investigating Monte Carlo data it was found that requiring an acoplanarity angle $\alpha = \angle((\overrightarrow{p}_{\pi_1} \times \overrightarrow{p}_{\pi_2}), (\overrightarrow{p}_{\pi_1} \times \overrightarrow{p}_{\omega})) > 5°$ rejects 90% of the two-pion background while only 17% of the ω-events are removed, thus improving the signal-to-background ratio. We would like to stress the robustness of the method as the selection of different acoplanarity angles result in the same yield of the ω-signal after acceptance correction, within an uncertainty of 2% [7]. Throughout the analysis an acoplanarity angle of $\alpha \geq 5°$ is required. Finally, in the analysis only those events are taken into account for which the sum of the proton momenta points into the backward hemisphere of the overall CMS in order to improve on the momentum resolution. Because of the identical particles in the entrance channel all distributions of final state particles in the overall CMS will be symmetric so that a reduction of information does not ensue.

In the present paper our former study [7] is buttressed by scrutinising the influence of the proton region chosen on the yield determined for the ω-signal. As already mentioned, three proton regions are considered, region A with rather narrow boundaries, a wider region B (formerly used in [7]) and an even larger one, region C. As shown in fig. 4, a distinctive peak at the ω-pole mass ($m_\omega =782.7$ MeV/c^2, [24]) can be seen in all cases above the multi-pion background, the shape of which for missing masses smaller than the ω-mass depends dramatically on the region chosen for the separation of protons and pions, while the shape above the ω-mass is barely different.

Region A, which sharply restricts the protons in angle and velocity, results in a missing mass spectrum where the shape of the background can hardly be estimated in the region of the ω-mass. The missing mass spectrum resulting from region B exhibits an ω-signal which resides on a smooth, apparently convex background which extends

to missing masses smaller than the ω-mass. When further enlarging the proton region to region C the background dominates the spectrum and its shape below the ω-signal tends to change from a convex to an almost linear shape. The advantage of using region B [7] lies in the best signal-to-background ratio, while in case of region C the ω-signal becomes less susceptible to the method used for its extraction (see below). This results in a smaller uncertainty for the extracted counts, although about 20% of the signal is lost. Thus, in contrast to our earlier analyses [7] we now use the wide region C which is adjusted with increasing excess energy in order to accommodate the protons which become less confined in angle and velocity. It is interesting to note that a signal of the η-meson appears at $550\,\mathrm{MeV}/c^2$, however, the excess energy of about 350 MeV in this channel causes a large width of this signal greatly complicating a detailed analysis of the data.

In order to quantitatively determine the yield of the ω-signal above background we follow two different approaches, briefly described in [19]. One method is a simultaneous least square fitting of a Voigt function (convolution of a Gaussian and a Breit-Wigner function) for the ω-signal and a second-order polynomial for the background below the signal. The width of the Breit-Wigner distribution is fixed to the natural width of the ω-meson ($\Gamma = 8.49$ MeV, [24]), while all other parameters are allowed to vary freely. The alternative method is based on the simulation of the main background channels (pp → ppρ, $\rho \to \pi^+\pi^-$, pp → pp$\pi^+\pi^-$, pp → pp$\pi^+\pi^-\pi^0$) where the simulated data are analysed in the very same way as the experimental data. The yield of various background contributions obtained are adjusted in order to reproduce the experimental background. It is found that the 3π-background dominates over the 2π-background (which was effectively reduced by the acoplanarity requirement); the non resonant 2π-contribution can be exchanged for the resonant one from ρ-decay as the ρ-meson has a large width. The result of both procedures is shown in fig. 5 for an excess energy of 128 MeV. The background described by the "pion-cocktail" agrees very well with the one determined by the fitting procedure. The yield determined for the ω-signal is found to agree within a few percent for the two methods; the present results are fully consistent with but more precise than our earlier ones. Although this experiment does not aim at a measurement of the ω mass we like to quote the parameters determined for the Voigt function at the three excess energies of $\varepsilon = 92, 128, 173\,\mathrm{MeV}$, namely $m_\omega = 780.2, 782.4, 779.5\,\mathrm{MeV}/c^2$ with a systematic uncertainty of 0.3% and a standard deviation of the Gaussian resolution function of $\sigma = 7.6 \pm 1.1, 10.3 \pm 0.5, 11.3 \pm 0.6\,\mathrm{MeV}/c^2$. As usual, the best momentum and, hence, mass resolution for time-of-flight experiments is achieved for the slowest particles, i.e. protons at the smallest excess energy.

The procedure of yield determination must be carried through for each interval of the differential observables, e.g. for different intervals in $\cos\theta^*_\omega$ to obtain the ω angular distribution in the overall CMS.
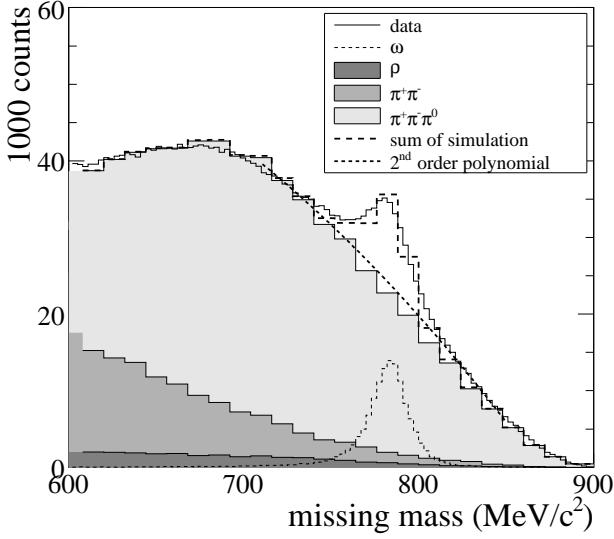
Fig. 5. Proton-proton missing mass spectra at $\varepsilon = 128$ MeV with adjusted Monte Carlo distributions obtained for resonant pp→ppρ, $\rho \to \pi^+\pi^-$ production and non-resonant two- and three-pion production. The sum describes the background below the ω-signal very well. (See text for details.)

The absolute normalisation is accomplished by evaluating elastic scattering, which is always measured simultaneously at COSY-TOF. The angular distribution determined is compared to literature data [25], whereupon the normalisation factor directly yields the integrated luminosity. The uncertainty of this procedure (5%) is in equal parts due to the intrinsic uncertainty of our measurement and the error of the literature data.

2.3 Monte Carlo simulations

During the analysis of the experimental data each step of the analysis was checked against results obtained by Monte Carlo simulations, thereby giving insight into the detector performance and, in particular, its acceptance. The programme package [26,27] models the whole COSY-TOF-detector in great detail (geometry of all sub-detectors, detector housings and wrappings, cabling, supporting structures etc.). The particles are generated according to equal population of phase space [28] and propagated in space and time accounting for small angle scattering, nuclear reactions, δ-electrons and energy loss in all detector components; the energy loss value is used to generate a charge or light output signal. The AD-conversion takes into account light attenuation in the hodoscopes, efficiency and gain of the individual photomultipliers. The time and charge resolution of the individual elements of different sub-detectors is also accounted for. A properly chosen amount of noise is added to each signal [29]. In addition, various decay anisotropies, e.g. that of the ω-decay ($J^P = 1^-$) can be included optionally [30]. The Monte Carlo simulations also account for the anisotropic $\cos\theta^*_\omega$ angular distributions as

experimentally observed (see section 3.2.1) at the three excess energies. These Monte-Carlo data are subjected to the very same analysis routines as the experimental data in order to treat both on an equal footing, thus, for all observables the detector acceptance can be determined. It is found that the acceptance is a smooth function for all differential observables as can be inferred from the figs. 7 to 15 shown below. The numerical value of the integral acceptance, however, depends largely on the size of region C chosen for proton identification and turns out to be slightly different for the three excess energies studied (see table 1).

2.4 Systematic uncertainties

Three major sources of systematic errors were identified for the present analysis. An obvious one is the uncertainty of the luminosity determination of 5% (see above). The second source of systematic uncertainties stems from the determination of the yield of the ω-signal residing on a sizable background. The acceptance correction itself is the third source of systematic uncertainties. The Monte Carlo simulation should model, besides other observables, the relation β vs θ_{lab} as perfectly as possible since it is used for particle identification. Although the majority of pions cluster at $\beta \approx 1$ some happen to fall into the β vs θ_{lab}-region chosen for proton assignment. This fraction is fairly sensitive to the correct simulation of the time resolution for pion tracks. Its influence can be studied by varying the β-boundary of the proton region. Thereby the systematic uncertainty of the acceptance correction was determined to amount to 4% at $\varepsilon = 92\,\mathrm{MeV}$ and $\varepsilon = 128\,\mathrm{MeV}$ and 6% at $\varepsilon = 173\,\mathrm{MeV}$.

In the case of the total cross section these three systematic uncertainties were added quadratically.

In case of differential cross sections the systematic uncertainties for the determination of the yield of the ω-signal and the acceptance correction were investigated in detail for each bin of the observable under consideration. A spread of uncertainties was quantified, firstly, by a systematic variation of the range of the missing mass included when fitting the background below and above the ω-signal and, secondly, by a comparison of the results obtained by the two different fitting methods. The spread was found to be between 5 and 20% and was added to the statistical error. The sum is indicated as a common error bar for each interval of the observable under consideration. The systematic error due to the luminosity determination contributes an overall uncertainty which is not shown.

## 3 Discussion of results

3.1 Total cross section

The number of ω-events extracted from the proton-proton missing mass spectrum at different excess energies are used to calculate the total cross sections listed in table 1.

Table 1. Total cross section for the reaction pp → ppω at three excess energies; N_ω: number of ω-events; acc: detector acceptance as determined from Monte Carlo simulations; see text for details.

ε (MeV)	N_ω	acc	$\int L \mathrm{d}t$ (μb^{-1})	$\sigma_{\rm tot}$ (μb)
92	2052	0.156	1449	$9.1 \pm 0.6 \pm 1.0$
128	116315	0.168	53500	$12.9 \pm 0.2 \pm 1.1$
173	3558	0.155	795	$28.9 \pm 1.9 \pm 3.1$

Table 2. Coefficients of Legendre polynomials determined by fitting eq.(2) to the ω angular distributions.

ε (MeV)	$\sigma_{\rm tot}$ (μb)	a_2'	a_4'
92	9.3 ± 1.1	0.23 ± 0.26	–
128	12.7 ± 0.5	0.49 ± 0.10	–
173	30.5 ± 1.8	0.46 ± 0.15	0.42 ± 0.18
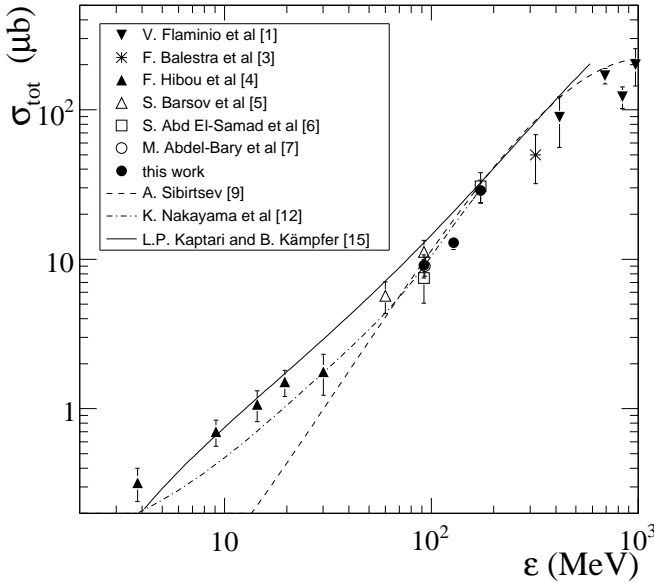
Fig. 6. Total cross section as a function of excess energy measured for the reaction pp → ppω.

The values at $\varepsilon = 92$ MeV and 173 MeV agree with those published earlier [6], [7], however with improved accuracy.

Fig. 6 shows all published data for this reaction; the present data follow the general trend. The results of theoretical models more or less follow the data, but the total cross section is not a sensitive observable that proves one or the other model preferable - additional observables are needed. As COSY-TOF almost completely covers the phase space of the reaction many differential cross section can be determined offering a variety of other physical quantities setting benchmarks for theoretical models. Hence we turn to differential distributions.

3.2 Angular distributions of the ω-mesons and protons in the overall CMS

3.2.1 ω-mesons

The ω angular distributions in the overall CMS are shown in fig. 7 for the three excess energies, the acceptance is shown in the lower part of each frame. It is a smooth function of $\cos\theta_\omega^*$ which drops with increasing angle only slightly from ≈40 to ≈30%. As pointed out above, the data analysis requires two protons with an added momentum

pointing into the backward hemisphere, hence we can show only the angular distribution for the forward hemisphere. A transition is observed from a slightly anisotropic to a pronounced anisotropic angular distribution.

The standard parametrisation of an angular distribution in the overall CMS in terms of Legendre polynomials reduces to

$$\frac{\mathrm{d}\sigma}{\mathrm{d}\Omega} = \sum_{L=0}^{L_{max}} a_{2L} \cdot P_{2L}, \quad L = 0, 1, 2, \ldots \quad (1)$$

since only even Legendre polynomials P_{2L} need to be taken into account in the case of identical particles in the entrance channel. This equation can be rearranged to

$$\frac{\mathrm{d}\sigma}{\mathrm{d}\Omega} = \frac{\sigma_{\rm tot}}{4\pi} \cdot (1 + \sum_{L=1}^{L_{\max}} a_{2L}' \cdot P_{2L}), \quad L = 1, 2, \ldots \quad (2)$$

where $\sigma_{\rm tot}/4\pi = a_0$ and $a_{2L}' = a_{2L}/a_0$. We prefer the use of eq.(2) over eq.(1) as the former yields the total cross section $\sigma_{\rm tot}$ without further calculation being necessary and the significance of the contributions of higher partial waves in the exit channel is better judged via the ratio a_{2L}' rather than a_{2L}. The coefficients obtained are listed in table 2.

While it is sufficient to use $L_{\max} = 1$ for the two lower excess energies, as can be deduced from table 2 the inclusion of $L_{\max} = 2$ improves the description of the angular distribution for $\varepsilon=173$ MeV although the uncertainty of a_4' is rather large. The values of $\sigma_{\rm tot}$ are consistent, within the uncertainties, with those listed in table 1. We like to point out that the deduced values of $L_{\max}$ are fully consistent with kinematic considerations: the maximal orbital angular momentum for the (pp)-ω system can be estimated as $\eta = p^*/m_\pi$ where p^* is the centre of mass momentum in the final state, $1/(2m_\pi)$ the strong interaction radius and m_π the pion mass [14]. For the three excess energies η varies from 2.4 to 3.3 $\hbar$. However, the angular momentum barrier truncates this maximum orbital angular momentum to an effective one of $L = 1\hbar$ for $\varepsilon = 92$ and 128 MeV, while $L = 2\hbar$ is only probable at $\varepsilon = 173$ MeV.

These results can be looked at from a different point of view. Meson production in pp reactions is usually described by defining the non-relativistic momenta **p** (relative momentum of the two protons) and **q** (momentum of the ω-meson with respect to the centre of mass of the two protons) and the associated orbital angular momentum quantum numbers L and l_ω, respectively. Then the spectroscopic notation $(^{2S+1}L_J)_i$ holds for the partial waves in the initial state and $(^{2S+1}L_J)_f \, l_\omega$ for the final state which
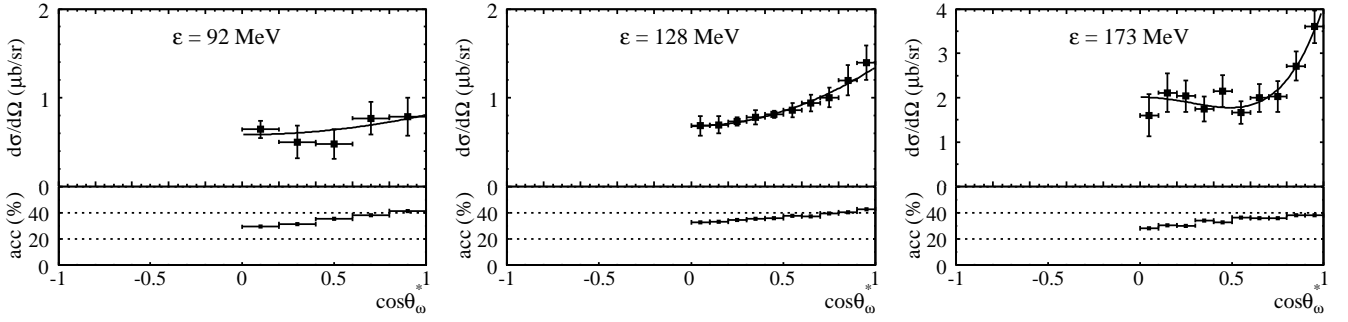
Fig. 7. Angular distribution of the ω-meson in the overall CMS (upper part in each frame). The lower part shows the acceptance of the COSY-TOF spectrometer as determined from Monte Carlo simulations.

Table 3. List of all partial waves in the initial state which can produce final states with two units of angular momentum at the most. The notation is defined in the text.

type	$(^{2S+1}L_J)_i \rightarrow (^{2S+1}L_J)_f l_\omega$	amplitude
Ss	$^3P_1 \rightarrow {}^1S_0\,s$	f_1
Sp	$^1S_0 \rightarrow {}^1S_0\,p$	f_2
	$^1D_2 \rightarrow {}^1S_0\,p$	f_3
Ps	$^1S_0 \rightarrow {}^3P_1\,s$	f_4
	$^1D_2 \rightarrow {}^3P_1\,s$	f_5
	$^1D_2 \rightarrow {}^3P_2\,s$	f_6
Sd	$^3P_2 \rightarrow {}^1S_0\,d$	f_7
	$^3F_2 \rightarrow {}^1S_0\,d$	f_8
	$^3F_3 \rightarrow {}^1S_0\,d$	f_9
Pp	$^3P_0 \rightarrow {}^3P_{0,1,2}\,p$	...
	$^3P_1 \rightarrow {}^3P_{0,1,2}\,p$	...
	$^3P_2 \rightarrow {}^3P_{0,1,2}\,p$	...
	$^3F_2 \rightarrow {}^3P_{0,1,2}\,p$	...
	$^3F_3 \rightarrow {}^3P_{1,2}\,p$	..
	$^3F_4 \rightarrow {}^3P_2\,p$	.
Ds	$^3P_2 \rightarrow {}^1D_2\,s$	f_{25}
	$^3F_2 \rightarrow {}^1D_2\,s$	f_{26}
	$^3F_3 \rightarrow {}^1D_2\,s$	f_{27}

in short will be designated as type "Ll_ω" later on; S, L, J refer to the quantum numbers of spin, orbital angular momentum, and total angular momentum of the pp-system in either initial (i) or final (f) state (see e.g. Hanhart [31]). We list in table 3 all partial waves of the entrance channel (antisymmetric pp-wave functions) which can produce (accounting for conservation of both parity and angular momentum) final states with at most two units of orbital angular momentum as suggested by the angular distribution of the ω-meson.

A comparison with the value of $L_{\max}$ deduced from the angular distribution shows that at $\varepsilon=92$ and 128 MeV final states of type Ss, Sp and Ps (amplitudes $f_1, f_2, .., f_6$) contribute, while at $\varepsilon=173$ MeV the final states of type Sd, Pp, and Ds (amplitudes $f_7, ..., f_{27}$) come into play. It is important to realise that from a particular initial state two or more final states can be populated (cf. amplitudes

Table 4. Coefficients of Legendre polynomials determined by fitting eq. (2) to the proton angular distributions.

| ε (MeV)	σ_{tot} (μb)	a_2'
92	8.5 ± 0.7	0.11 ± 0.22
128	12.7 ± 0.3	0.12 ± 0.06
173	27.8 ± 1.3	0.13 ± 0.11

f_2 and f_4 or f_3, f_5, and f_6). Which of these amplitudes are present in the reaction and contribute with which weight depends on the transition matrix elements; they can be determined by a full model calculation. However, we conjecture that, due to the available excess energy, the two final state protons are most probably in the $^1S_0$ state. This would reduce the mainly contributing final states to those of type Ss, Sp, and Sd. It cannot be excluded that final states of type Ps are present as they originate from the same initial state as Sp type states, but probably with only little weight.

3.2.2 Protons

In fig. 8 we show the angular distributions of protons in the overall CMS for the three excess energies. The acceptance (lower part of each frame) is a smooth function of $\cos \theta_{\text{p}}^*$ with an almost constant slope. The decrease towards $\cos \theta_{\text{p}}^* = 1$ is due to the analysis requirement of the sum of the proton momenta pointing into the backward direction. The angular distributions are, within uncertainties, symmetric with respect to $\cos \theta^* = 0$, as they should be in the case of identical particles in the entrance channel. This is a strong indication that the acceptance corrections were performed properly.

Using even Legendre polynomials (P_0 and P_2) according to eq. (2) the least square fitting resulted in the values of table 4. The distributions are almost isotropic; little room is left for an $L = 1$ partial wave. As a consequence, the final state pp-system is most probably in the $^1S_0$-state and less probably in the ^3P-state; this conclusion is consistent with that drawn from the ω angular distribution.

As mentioned in the introduction, there are theoretical models which favour ω-production to proceed via N^*-resonances (pp $\rightarrow$ pN^*, $N^* \rightarrow$ pω). The finding of an
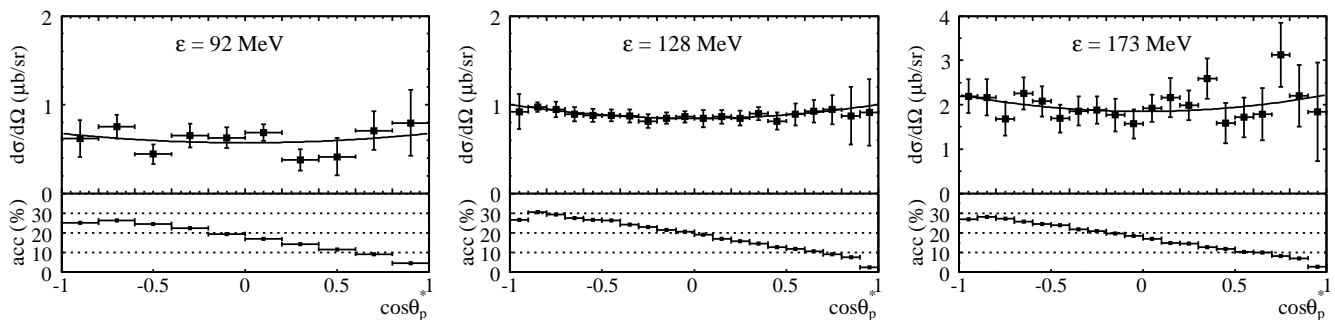
Fig. 8. Angular distribution of the protons in the overall CMS (upper part in each frame). The lower part depicts the acceptance of the COSY-TOF spectrometer as determined from Monte Carlo simulations.

isotropic, at most slightly anisotropic proton angular distributions at all energies and that of undeniably anisotropic ones for ω-mesons at the two higher excess energies are difficult to reconcile with resonant ω-production as the major reaction mechanism. This will be shown in the following discussion.

In the present experiment the mass region of 1.721 GeV/c^2 (threshold) to 1.893 GeV/c^2 (highest beam momentum) was covered. In this region nucleon resonances are known which have significant $N^* \to p\omega$ decay branches, namely N(1710)P$_{11}$, N(1720)P$_{13}$, and N(1900)P$_{13}$ [24]. Below the threshold N(1535)S$_{11}$, N(1650)S$_{11}$, N(1675)D$_{15}$, N(1680)F$_{15}$, and N(1700)D$_{13}$ are listed in [24]. Most of them are classified as four star resonances, while N(1700) and N(1710) have three and N(1900) two stars. Above the accessible mass range the two star resonances N(1990)F$_{17}$, N(2000)F$_{15}$, N(2080)D$_{13}$ are located. All these N^* resonances have large widths of typically 100 - 200 MeV and, hence, their Breit-Wigner tail may well extend into the mass interval covered by this experiment. The inclusion of subthreshold resonances has proven important in the calculation of coupling constants of baryon resonances to the nucleon-omega channel in particular the subthreshold resonances S$_{11}$ and D$_{13}$; above the ω-threshold N(2080)D$_{13}$ was found to be of particular importance [32]. It should also be stressed that the N(1535)S$_{11}$ resonance was specifically claimed to play a crucial role in off-shell ω-production [13]. Hence, in order to be as unbiased as possible, we include all of these resonances in the following consideration on resonant ω-production.

In the case of the pp → pN^*, $N^* \to p\omega$ reaction the CMS angular distribution of the proton associated with the N^*-resonance depends on spin and parity of the N^*-resonance and can be calculated using the formalism developed for nuclear reactions by Blatt and Biedenharn [33]. They showed that the transition from an initial state with $J = L_i + S_i$ to a final state with $J = L_f + S_f$ (here the final state is the pN^* system) is characterized by an angular distribution which can be described by an expansion in even Legendre polynomials P_L in analogy to eq. (1). The expansion coefficients are uniquely determined for a given set of quantum numbers L_i, S_i, J, L_f, S_f from Wigner and Clebsch-Gordan coefficients. The maximum of the summation index is L_{max} which, in the case

of reactions with integer values of J, is given by $L_{max}=\min(L_i, J, L_f)$. Examples of angular distributions for protons from the pp → pN^*(1720) reaction for various sets of quantum numbers (L_i, S_i, J, L_f, S_f) can be found in [14].

We used this formalism [33] to find those pp → pN^*-reactions which show isotropic proton angular distributions. They are obtained only for transitions from the initial states ^{1}S$_0$ or ^{3}P$_0$ to any N^*-resonance and from ^{3}P$_1$ to S$_{11}$. This is the consequence of either L_i, J or L_f being zero, thus $L_{max} = 0$. Then, whatever resonance is involved, the angular distribution of the decay products is isotropic. Thus we have pinned down three initial states which can lead via resonant ω-production to both isotropic proton and ω angular distributions.

All other initial states result in angular distributions of various degree of anisotropy in the production step. In particular the transitions from initial states ^{3}P$_1$ and ^{3}P$_2$ (amplitudes f_1 and f_7 of table 3) to any N^*-resonance (except ^{3}P$_1$ to S$_{11}$ which is isotropic) give angular distributions of the type $a_0 + a_2P_2$. If the N^*-resonance now decays isotropically, then the anisotropy from the production process is diluted. As N^*-resonances such as P$_{11}$ and P$_{13}$ decay with a relative angular momentum of $1\hbar$, the anisotropy from the production process may be enhanced. This applies to the resonances N(1710)P$_{11}$, N(1720)P$_{13}$, and N(1900)P$_{13}$ in the mass region accessible in this experiment. We conclude that resonant ω-production can produce isotropic as well as anisotropic angular distributions for protons and ω-mesons, however the degree of anisotropy at $\varepsilon = 92$MeV indicates that this contribution is of minor weight. It is also conceivable that resonant production provides a minor contribution at the higher energies.

The initial states not mentioned explicitly so far yield proton angular distributions from the production step that are of the type $a_0 + a_2P_2 + a_4P_4$ and may even include an a_6P_6 term. This implies also an anisotropic sequential N^*-decay, and hence, anisotropic ω angular distributions are expected. We are not aware of any mechanism that would yield isotropic proton angular distributions when superimposing those of anisotropic production and anisotropic sequential decay. Hence we conclude that the isotropic proton angular distributions and the strongly anisotropic ω angular distributions observed at the higher excess ener-

gies are incompatible with resonant ω-production dominating the reaction mechanism.

We summarise the conclusions drawn from the interpretations of the angular distributions of ω-mesons and protons in the overall CMS: the former are produced with exit channel angular momenta of 0, 1, and 2 $\hbar$ depending on excess energy while protons are found to be emitted almost isotropically at all excess energies. This implies that protons are produced most probably in the $^1S_0$ (amplitudes $f_1, f_2, f_3, f_7, f_8, f_9$ of table 3), and less probably in the ^3P final state (amplitudes f_4, f_5, f_6). The contribution of the other amplitudes is assumed to be insignificant. The definite anisotropy of the ω angular distribution and the almost isotropic proton angular distribution observed at $\varepsilon = 128$ and 173 MeV rules out resonant ω-production to be the major reaction mechanism at these excess energies. It cannot be excluded that it contributes to the angular distributions of ω-mesons and protons to a minor extent at all excess energies as resonant ω-production via the N^*-resonances S_{11}, D_{13} yields isotropic and via P_{11} or P_{13} anisotropic angular distributions. In these cases, only particular initial states contribute.

3.3 Orientation of the ω-spin

Already in 1962 it has been pointed out by Gottfried and Jackson [34] that the orientation of the ω-spin gives valuable information on the reaction mechanism of ω-production. The orientation of the ω-spin is correlated with that of the decay plane of the ω meson. The latter can be determined from the pion momenta in the CMS of the decaying ω-meson. In our experiment the two protons and the charged pions are detected, however the momentum resolution for these fast pions ($\beta \approx 1$) is not sufficient to make direct use of the measured momenta such as to calculate the missing 4-momentum of the π^0. Nevertheless, its 4-momentum can be determined by exploiting the time of flight of the two observed pions, $TOF_{\text{obs},\pi}$, and the ω-momentum. The latter is known as $p_\omega = p(\text{pp}_{\text{initial}}) - p(\text{pp}_{\text{final}})$ and the 4-momenta of all three pions must add up to $p_\omega = p_{\pi^-} + p_{\pi^+} + p_{\pi^0}$. By varying the 4-momenta of the charged pions and calculating the corresponding time of flight, $TOF_{\text{calc},\pi}$, one can find that momentum partition which yields the minimum deviation $(\Delta TOF)^2 = (TOF_{\text{calc},\pi_1} - TOF_{\text{obs},\pi_1})^2 + (TOF_{\text{calc},\pi_2} - TOF_{\text{obs},\pi_2})^2$. This method allows to deduce all pion momenta and thus the orientation of the ω decay plane which is determined with an accuracy of $\sigma = 10°$. We like to point out, however, that this analysis cannot be used to improve on the ω-signal as the background below the signal cannot be reduced.

It was pointed out by Gottfried and Jackson [34] and later on by Titov et al. [16], [35] that it is essential to specify the reference frame within which an observable is measured. These authors showed that for the reaction $pp \to pp\phi, \phi \to K^+K^-$ the decay angle θ, defined as the polar angle of the direction of flight of one of the decay particles in the ϕ-meson's rest frame with respect to the

beam direction, shows an angular distribution (normalised to 1) given by

$$W(\cos\theta) = \frac{3}{4}(1 - \rho_{00} + (3\rho_{00} - 1)\cos^2\theta) \qquad (3)$$

If ϕ-production is considered just above threshold the spin of the ϕ-meson is aligned and the spin density matrix element $\rho_{00} = 0$; then eq.(3) reduces to

$$W(\cos\theta) = \frac{3}{4}\sin^2\theta \qquad (4)$$

This relation was used by e.g. Balestra et al. [3], Rekalo et al. [36] and Hartmann et al. [37] in their investigations of the spin alignment of the ϕ-meson.

The appropriate reference axis for the 3-body decay of the ω-meson is the normal to the decay plane. The angle of the normal with respect to the beam axis becomes $\gamma = \pi/2 - \theta$ and replaces the angle θ in eq.(3) when translating the 2-body ϕ-decay into the 3-body ω-decay. Eq.(3) then reads

$$W(\cos\gamma) = N(1 - \rho_{00} + (3\rho_{00} - 1)\sin^2\gamma)$$
$$= N(2\rho_{00} - (3\rho_{00} - 1)\cos^2\gamma) \qquad (5)$$

with the proper normalisation constant $N = 1/(2\rho_{00} + 2/3)$.

We will exploit the eq.(5) in order to investigate a possible spin alignment in the ω-production. The term alignment arises from the following consideration: the orbital angular momentum of the initial state of the $pp \to pp\omega$ reaction is always oriented perpendicularly to the beam and the projection quantum number of the total angular momentum M_{J_i} of the pp-system can only assume the values of 0 or ± 1 as the Clebsch-Gordan coefficients show. The restriction $M_{J_i} = 0, \pm 1$ carries over to the final state, and the notion of an aligned total angular momentum applies if $M_{J_f} = \pm 1$ only.

Directly at threshold, the transition $^3P_1 \to {}^1S_0$s (amplitude f_1 of table 3) is the only possible one. In this case, $J_i = J_f = s_\omega = 1$ and $M_{J_i} = m_{s_\omega} = \pm 1$, i.e. the spin of the ω-meson is aligned (which goes along with $\rho_{00} = 0$) and the angular distribution becomes according to eq. (5)

$$W(\cos\gamma) = \frac{3}{2}\cos^2\gamma \qquad (6)$$

This finding, solely based on conservation laws which are reflected by the appropriate Clebsch-Gordan coefficients, is true independent of the reaction model under consideration.

It should be pointed out, that $\rho_{00} = 0$ holds only at threshold but assumes values of about 0.2 already slightly above. This is a consequence of the spin-orbit interaction [38]. Naturally, this effect increases with the vector meson momentum $\boldsymbol{q}$.

Above threshold, we have to consider firstly, Sp type final states (amplitudes f_2 and f_3 of table 3). For the amplitude f_2 the initial state $^1S_0$ does not exhibit any orientation, hence the ω-spin has no particular orientation and $W(\cos\gamma) = 1/2$ is isotropic. This reflects the fact that all

Table 5. Parameters of the function eq.(7) used to describe the distribution of the angle γ between the normal on the ω-decay plane and the beam-axis.

ε (MeV)	σ_{tot} (μb)	ρ_{00}
92	8.3 ± 1.2	0.17 ± 0.07
128	12.0 ± 0.6	0.19 ± 0.03
173	28.0 ± 2.3	0.24 ± 0.05

spin projection states are equally populated and, hence, the spin density matrix element $\rho_{00} = \rho_{11} = \rho_{-1-1} = 1/3$. For the amplitude f_3 ($^1D_2 \to {}^1S_0$p) one finds $M_{J_f} = 0$, i.e. the total angular momentum of the ω-meson is perpendicular to the beam axis. The ω-spin projection quantum number, however, can assume the values $m_{s_\omega} = 0, \pm 1$ resulting in a distribution of the type $a \cdot \sin^2\gamma + b \cdot \cos^2\gamma$ which tends to reduce the anisotropy due to amplitude f_1. Secondly, we consider Sd type final states. Distributions of the same type as for amplitude f_3 are expected. Thirdly, if we take into account Ps type final states we find isotropy for amplitude f_4, type $a \cdot \sin^2\gamma + b \cdot \cos^2\gamma$ distributions for f_5 and alignment for f_6.

The measured angular distribution of the ω-spin direction is shown in fig. 9. We describe these angular distributions by employing eq.(5)

$$\frac{d\sigma}{d\cos\gamma} = \frac{\sigma_{tot}}{2\rho_{00} + 2/3}(2\rho_{00} - (3\rho_{00} - 1)\cos^2\gamma). \quad (7)$$

Fig. 9 depicts the results of the fitting as a solid line. The values determined for σ_{tot} and (ρ_{00}) are listed in table 5.

The increasing value of ρ_{00} indicates the transition from an aligned ω-spin ($\rho_{00} = 0$) to an arbitrarily oriented ω-spin ($\rho_{00} = 1/3$). This is due to two effects, firstly the increasing importance of reaction amplitudes that show no alignment, namely those of the initial state $^1S_0$ which provide an isotropic contribution to the angular distribution as well as those which feature a $\sin^2\gamma$-dependence, and secondly the the above mentioned increase of ρ_{00} due to spin orbit interaction being important above threshold [38]. The energy dependence of the parameter ρ_{00} sets a benchmark for theoretical models of ω-production.

3.4 Invariant mass spectra

Invariant mass spectra of the two-body subsystems can be used to search for deviations from phase space which would be indicative of a resonance. In order to determine an invariant mass spectrum the ω-signal needs to be extracted from the missing mass spectra generated for various bins in the invariant mass. It turned out that this was possible only if a Monte Carlo simulated pion-cocktail was used for the determination of the background. The statistical basis of our data does not allow to generate a Dalitz plot.

The results obtained are shown in figs. 10 and 11 (upper part of each frame, the lower part shows the acceptance) together with the simulated distribution based on an equally populated phase space for the ω-production. The fuzzy fringes of the simulated distributions (upper end of M_{pp} and lower end of $M_{\omega p}$) reflect the finite width of the ω-meson; the experimental data are reproduced very well. N^*-resonances with widths in the order of 100 to 200 MeV do not cause the invariant mass spectrum to deviate perceptibly from phase space, as simulations have shown. Arguing the other way around we conclude that any resonance with a width below our missing mass resolution of 10 MeV would show up if their cross section would be above $\approx 0.5\mu$b.

It is obvious from these results that indications of resonant ω-production are missing. This finding is compatible with that from the investigation of the proton angular distributions. An observable closely related to the invariant mass will be discussed in the following subsection.

3.5 Helicity and Jackson angle

3.5.1 Notation

In a $2 \to 3$ reaction ($a + b \to 1 + 2 + 3$) with conservation of 4-momentum given by

$$p_a + p_b = p_1 + p_2 + p_3 \quad (8)$$

the initial state in the overall CMS is defined by a direction and the total energy $\sqrt{s}$ which both are known in standard collision experiments. The description of the final state requires $3 \times 3 = 9$ variables (besides the masses in the exit channel) which, due to conservation of momentum and energy, reduce to five variables. Without polarisation in the entrance channel the azimuthal orientation of the final state is arbitrary, reducing the number of necessary variables to four.

The four variables needed to uniquely describe the reaction can be represented by two invariants and two angles. For the latter one may choose e.g. the CMS angles of any two final state particles; for the invariants one often chooses the invariant masses of 2-body subsystems

$$s_{13} = (p_1 + p_3)^2 = (p_a + p_b - p_2)^2 \quad (9)$$
$$s_{23} = (p_2 + p_3)^2 = (p_a + p_b - p_1)^2 \quad (10)$$

where s_{12} may be chosen as an alternative to s_{13} or s_{23}. With this choice, only quantities of the exit channel are taken into account. This shortcoming can be avoided by choosing a suitable angle in an appropriate Lorentz reference system [34]. The latter is obtained by boosting the final state in such a way that the momenta of particle 2 and 3 add up to zero; one then obtains from eq. (8)

$$0 = \boldsymbol{p}_2 + \boldsymbol{p}_3 = \boldsymbol{p}_a + (\boldsymbol{p}_b - \boldsymbol{p}_1) = \boldsymbol{p}_b + (\boldsymbol{p}_a - \boldsymbol{p}_1). \quad (11)$$

Now, an angle connecting exit and entrance channel is the (polar) Jackson angle (notation of Byckling and Kajantie [39])

$$\cos\theta_{b3}^{R23} = \frac{\boldsymbol{p}_b \cdot \boldsymbol{p}_3}{|\boldsymbol{p}_b| \cdot |\boldsymbol{p}_3|}\Big|_{\boldsymbol{p}_2 = -\boldsymbol{p}_3}. \quad (12)$$
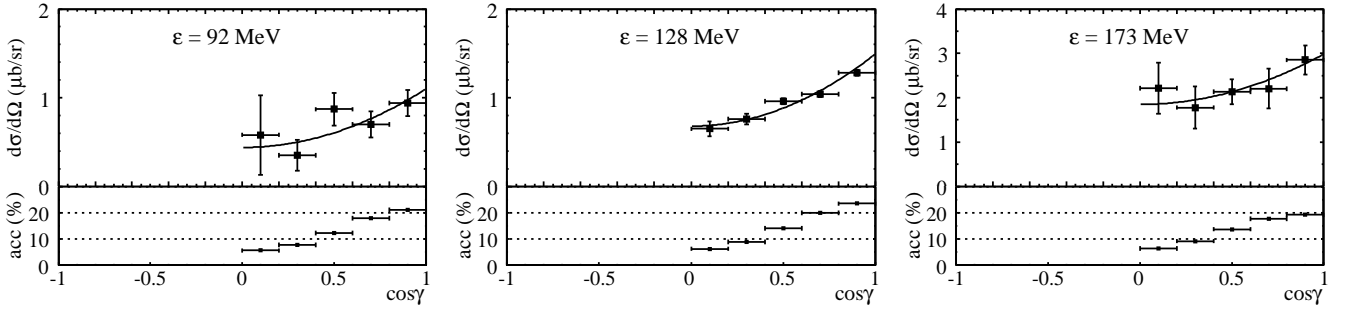
Fig. 9. Distributions of the angle between the direction of the ω-spin and the beam axis at the three excess energies (upper part in each frame; lower part: acceptance). See text for details.
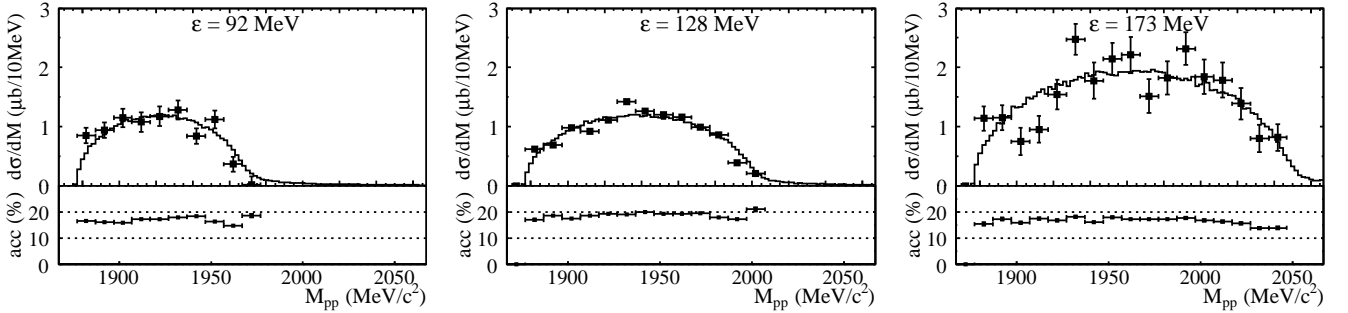
Fig. 10. Invariant pp-mass distribution (upper part of each frame, acceptance: lower part). The histograms represent the phase space distributions.

Fig. 11. Invariant ωp-mass distribution (upper part of each frame, acceptance: lower part). The histograms represent the phase space distributions.
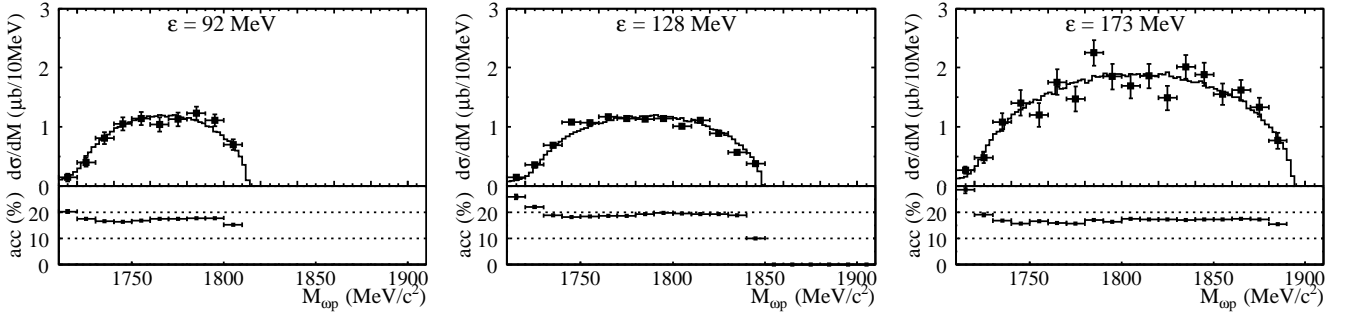
The superscript specifies the Lorentz reference system R23 chosen through $\boldsymbol{p}_2 = -\boldsymbol{p}_3$; the first subscript indicates which particle defines via its momentum direction the polar reference axis (a or b for the Jackson frame). The second subscript specifies which particle is used when calculating the Jackson angle. Since $\boldsymbol{p}_2 = -\boldsymbol{p}_3$, the choice of this particle is arbitrary, and $\theta_{b3}^{\mathrm{R23}} = \pi - \theta_{b2}^{\mathrm{R23}}$.

In the same Lorentz reference system one can also calculate the (polar) helicity angle

$$\cos \theta_{13}^{\mathrm{R23}} = \frac{\boldsymbol{p}_1 \cdot \boldsymbol{p}_3}{|\boldsymbol{p}_1| \cdot |\boldsymbol{p}_3|}\bigg|_{\boldsymbol{p}_2 = -\boldsymbol{p}_3}. \qquad (13)$$

which, in contrast to the Jackson angle depends on exit channel properties only. Again the Lorentz reference system "R23" chosen through $\boldsymbol{p}_2 = -\boldsymbol{p}_3$ is specified by the

superscript, while the first subscript indicates which particle defines via its momentum direction the polar axis (1 for the helicity frame). The second subscript specifies which particle is used when calculating the helicity angle. Since $\boldsymbol{p}_2 = -\boldsymbol{p}_3$, the choice of this particle is arbitrary, and $\theta_{13}^{\mathrm{R23}} = \pi - \theta_{12}^{\mathrm{R23}}$. Of course, all formulae are also valid for any other Lorentz reference systems (superscript R12 or R13 in eq.(12) or eq.(13) with the corresponding first and second subscript.

3.5.2 Helicity angle

The helicity angle relates particles 2 and 3 to particle 1, and hence carries information solely about the exit channel. This information is also contained in the Dalitz-plot:
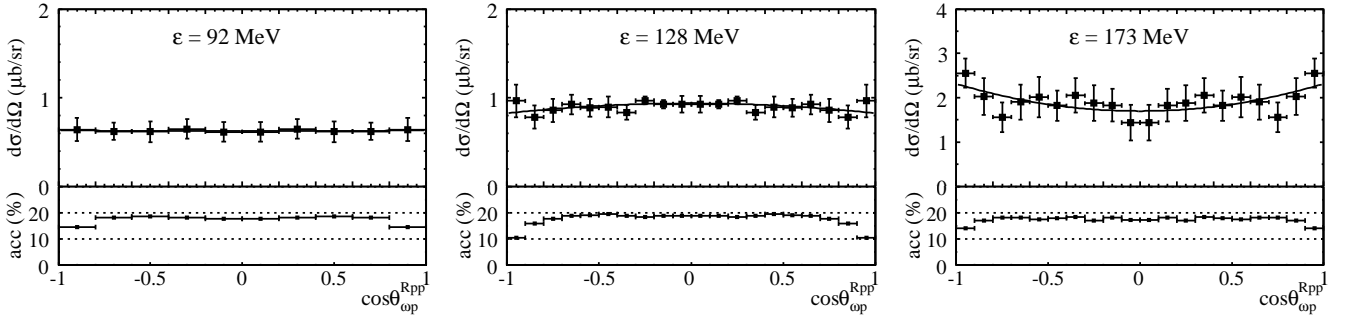
Fig. 12. Helicity angle distribution of the ω-meson in the pp-helicity frame (upper part of each frame, acceptance: lower part).
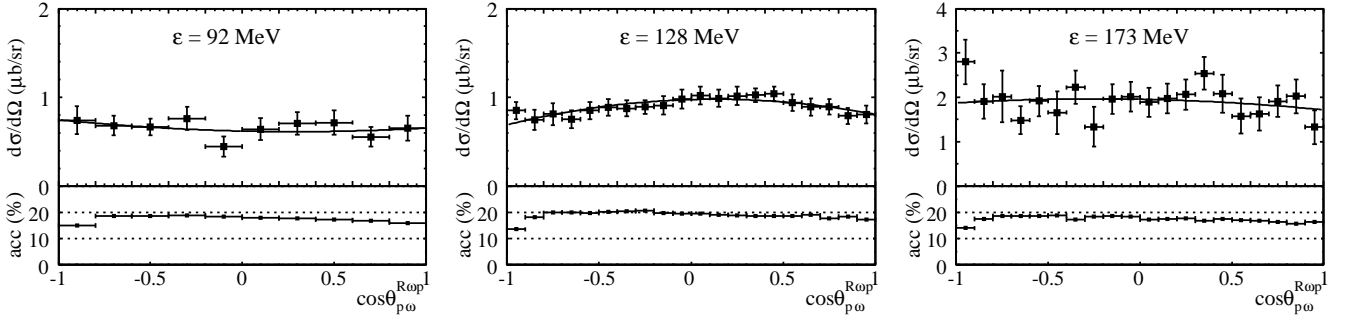
Fig. 13. Helicity angle distribution of the "other" proton in the ωp-helicity frame (upper part of each frame, acceptance: lower part).
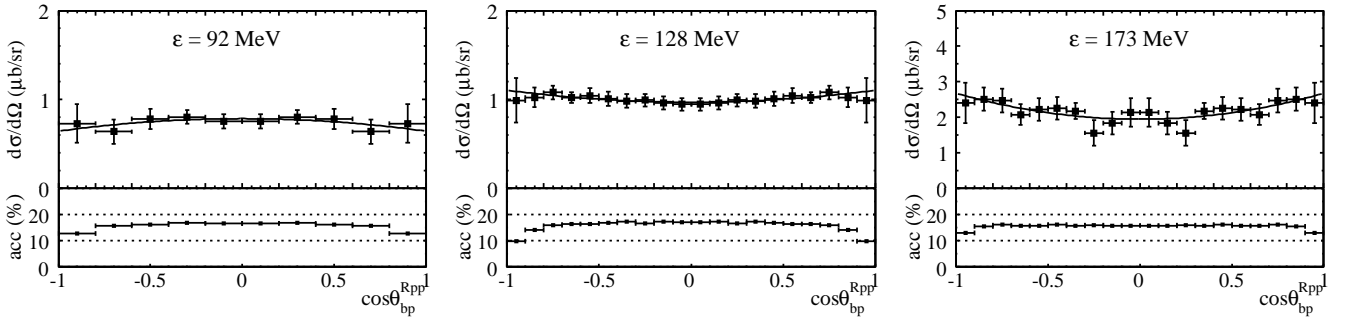
Fig. 14. Distribution of the angle between the beam direction and that of a proton in the pp-Jackson frame (Jackson angle) (upper part of each frame, acceptance: lower part).
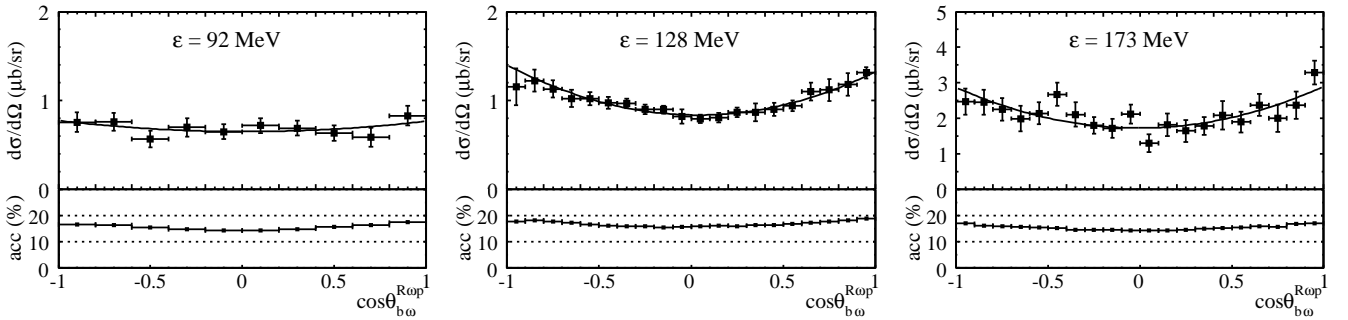
Fig. 15. Distribution of the angle between beam and the ω-meson in the ωp-Jackson frame (Jackson angle) (upper part of each frame, acceptance: lower part).

A resonance in the 2-3-system is observed as an enhancement of events along the s_{23}-axis at a certain mass and the distribution of $\cos\theta_{13}^{R23}$ is simultaneously seen along the s_{13}-axis. From this helicity angle distribution the spin of the resonance can be inferred in particular cases. It should be noted that this angular distribution is not necessarily symmetric with respect to $\cos\theta_{13}^{R23} = 0$ as it does not relate to the entrance channel.

Two helicity angles can be considered for the reaction pp → ppω: In the first case the two protons are used to define the Lorentz reference system and the polar helicity angle of the ω-meson is determined with respect to one of the protons. Since the two protons are indistinguishable we must take into account two distributions, namely $\theta_{\omega p_1}^{\mathrm{Rpp}}$ and $\theta_{\omega p_2}^{\mathrm{Rpp}}$. This results in a symmetrised helicity angle distribution.

The result is shown in fig. 12 where all possible values of s_{12} are accounted for. This corresponds to a summation of Dalitz-plot entries with constant values of $\cos\theta_{\omega p}^{\mathrm{Rpp}}$. The solid lines represent the results of least square fitting using eq.(2). The coefficients are listed in the first section of table 6.

At $\varepsilon = 92$ MeV one observes isotropy as well as at $\varepsilon = 128$ MeV. At $\varepsilon = 173$ MeV the increase of cross section at $\cos\theta_{\omega p}^{\mathrm{Rpp}} = \pm 1$ seems to indicate that the ω-meson has some tendency to move along with a proton. This may reflect the angular momentum of the ω-meson with respect to the $^1S_0$ di-proton and not necessarily a contribution of a resonance. A theoretical model is asked for to explain this observation.

In the second case one proton (for instance particle 2) and the ω-meson (particle 3) are used to define the Lorentz reference system, and the polar helicity angle of the other proton (particle 1) is determined with respect to the direction of the ω-meson. Since the two protons are indistinguishable we must average the distributions of $\theta_{p_2\omega}^{\mathrm{R\omega p_1}}$ and $\theta_{p_1\omega}^{\mathrm{R\omega p_2}}$ for a given event. A possible anisotropy in the helicity angle is not destroyed by this procedure.

Fig. 13 shows this helicity angle distribution where all possible values of s_{23} were taken into account. This corresponds to a summation of Dalitz-plot entries with constant values of $\cos\theta_{p\omega}^{\mathrm{R\omega p}}$. The solid lines represent the results of least square fitting using eq.(2) but allowing P_1 in addition with a weight of $a_1' = a_1/a_0$. The coefficients are listed in the second section of table 6.

The helicity angle distributions at $\varepsilon = 92$ and 173 MeV are isotropic within uncertainties. At $\varepsilon = 128$ MeV significant anisotropy and asymmetry values are observed pointing at an inhomogeneous population of the Dalitz plot which is probably caused by the angular momentum in the exit channel. This finding, however, is not in contradiction with the helicity angle distribution of fig. (12) as a different projection of the Dalitz plot is presented. Again, without a theoretical model one cannot explain the origin of this effect.

3.5.3 Jackson angle

The Jackson angle relates the direction of the beam momentum with the orientation of the axis given by $\boldsymbol{p}_2 = -\boldsymbol{p}_3$. Eq.(11) can be interpreted, as suggested by Gottfried and Jackson [34], as a 2 → 2 reaction, namely $2+3 \to b+x$ where particle x with $p_x = p_a - p_1$ can be identified with the exchange meson in diagram (a) or (c) in fig. 1. Thus it is clear that any structure in the Jackson angle distribution gives direct information on the angular momentum of the system R23 which could, but not necessarily has to, be a resonance [40].

Two Jackson angles can be considered for the reaction pp → ppω: In the first case the two protons (particle 1 and 2) are used to define the Lorentz reference system and the angle between the direction of one of the two protons with respect to the beam direction is called the polar Jackson angle. Since the protons are indistinguishable we must take into account the angles $\theta_{bp_1}^{\mathrm{Rpp}}$ and $\theta_{bp_2}^{\mathrm{Rpp}}$, a procedure which leads to a distribution of a symmetrised polar Jackson angle $\theta_{bp}^{\mathrm{Rpp}}$. Since beam and target proton can not been distinguished, both Jackson angles with respect to beam and target are taken into account for each event (maintaining for simplicity the sudscript b in $\theta_{bp}^{\mathrm{Rpp}}$)

In fig. 14 we show this symmetrised Jackson angle distribution. The solid lines represent the results of least square fitting using eq.(2). The coefficients are listed in the third section of table 6.

The fits suggest a slight anisotropy which implies that there is at most a very weak correlation between the beam direction and the final proton pair. This is compatible with the proton angular distributions presented in fig. 8 which showed an insignificant contribution of Ps type final states.

In the second case one proton (for instance particle 1) and the ω-meson (particle 3) are used to define the Lorentz reference system, and the polar Jackson angle is measured as the direction of the ω-meson with respect to the beam direction. Since the two protons in the exit channel are indistinguishable we must average the angles $\theta_{b\omega}^{\mathrm{R\omega p_1}}$ and $\theta_{b\omega}^{\mathrm{R\omega p_2}}$ in order to yield $\theta_{b\omega}^{\mathrm{R\omega p}}$. This averaging causes a dilution of a signal from a potential resonance since this is either found in the ωp_1 or ωp_2 system, while the non-resonant one furnishes an uncorrelated, hence isotropic background.

Again, the indistinguishability of beam and target are taken into account. However, in the Lorentz reference system beam and target momenta are not aligned, hence this procedure is not a symmetrisation, but the distribution turns out to be symmetric.

In fig. 15 we show this Jackson angle distribution. The solid lines represent the results of least square fitting using eq.(2). The coefficients are listed in the fourth section of table 6.

The Jackson angle distribution at $\varepsilon = 92$ MeV is almost isotropic but pronounced anisotropies are observed at the other excess energies beyond doubt. This shows that there is a non-zero relative angular momentum in the ωp system. However, a conclusion that this is a direct signal

Table 6. Coefficients of Legendre polynomials determined by fitting eq.(2) to the distributions of the different observables.

observable	ε (MeV)	σ_{tot} (μb)	a_1'	a_2'
$\cos\theta_{\omega\mathrm{p}}^{\mathrm{Rpp}}$ (fig. 12)	92	8.8 ± 0.5	–	0.01 ± 0.14
	128	12.7 ± 0.3	–	-0.08 ± 0.07
	173	26.8 ± 1.2	–	0.22 ± 0.10
$\cos\theta_{\mathrm{p}\omega}^{\mathrm{R}\omega\mathrm{p}}$ (fig. 13)	92	9.1 ± 0.5	-0.07 ± 0.11	0.08 ± 0.15
	128	12.7 ± 0.3	0.07 ± 0.04	-0.17 ± 0.06
	173	26.8 ± 1.2	-0.04 ± 0.08	-0.06 ± 0.11
$\cos\theta_{\mathrm{bp}}^{\mathrm{Rpp}}$ (fig. 14)	92	9.2 ± 0.5	–	-0.13 ± 0.15
	128	12.7 ± 0.2	–	0.09 ± 0.05
	173	27.5 ± 0.9	–	0.22 ± 0.09
$\cos\theta_{\mathrm{b}\omega}^{\mathrm{R}\omega\mathrm{p}}$ (fig. 15)	92	8.7 ± 0.4	-0.01 ± 0.08	0.12 ± 0.11
	128	12.7 ± 0.2	-0.04 ± 0.04	0.35 ± 0.04
	173	26.5 ± 0.9	0.01 ± 0.06	0.37 ± 0.08
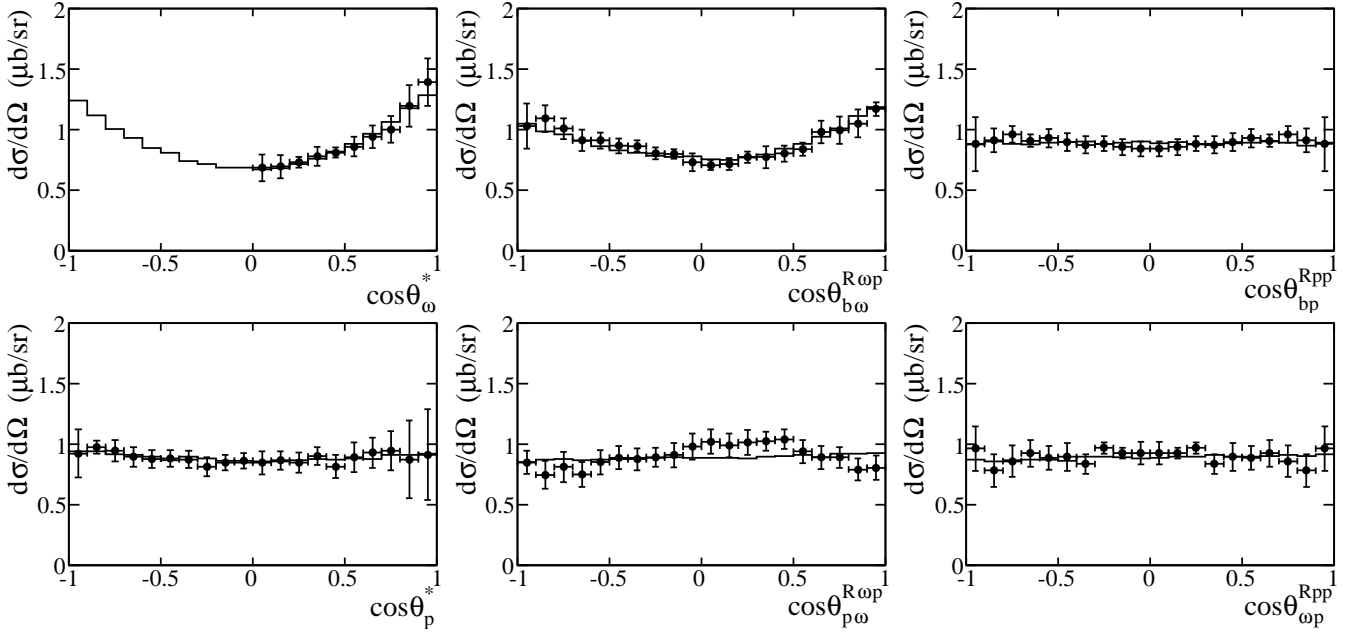
Fig. 16. Comparison of the experimental results with a Monte Carlo simulation using the measured distribution of $\cos\theta_\omega$ as a weight function.

of a N^*-resonance decaying into pω should be drawn with caution. The deduced values of $L = 0, 1, 2$, as discussed in the context of the ω angular distributions (fig. 7), are reflected by the Jackson angular distribution. In order to corroborate this argument we present in fig. 16 (together with data already shown) results of Monte Carlo simulations at $\varepsilon = 128$ MeV where the event generator was modified such as to reproduce the ω angular distribution of fig. 7, again shown in the upper left frame of fig. 16. This weight function on the ω angular distribution also modifies the proton angular (lower left) and Jackson angle distributions (upper middle and right frame) in such a way that they perfectly match the experimental ones. We obviously observe in the Jackson angle distribution the deviation of the reaction kinematics from pure phase

space. The helicity angle distributions (lower middle and lower right frame), however, cannot be reproduced.

We tentatively conclude that we observe the influence of some particular reaction dynamics: the transition matrix element connecting the initial with the final state shows a dependence on $\boldsymbol{q}$ and l_ω but not on $\boldsymbol{p}$ or L, creating anisotropic angular distributions of the ω-mesons, helicity angle $\theta_{\mathrm{p}\omega}^{\mathrm{R}\omega\mathrm{p}}$, and Jackson angle $\theta_{\mathrm{b}\omega}^{\mathrm{R}\omega\mathrm{p}}$. The final state protons are in the $^1\mathrm{S}_0$ state, resulting in isotropic angular distributions of θ_{p}^*, helicity angle $\theta_{\omega\mathrm{p}}^{\mathrm{Rpp}}$, and Jackson angle $\theta_{\mathrm{bp}}^{\mathrm{Rpp}}$.

We would like to note that the results of the corresponding investigation at $\varepsilon = 173$ MeV allow the same conclusion.

4 Summary

In this paper we presented a systematic study of the production of ω-mesons in proton-proton-collisions, carried out in a kinematically complete experiment at three excess energies of $\varepsilon = 92, 128, 173$ MeV. The large-acceptance COSY-TOF spectrometer allows the almost unambiguous and simultaneous identification of different reaction channels. We described in detail how the yield of ω-events was determined in the presence of an unavoidable physical background which is due to the production and decay of the ρ-meson ($\rho \to \pi^+\pi^-$) and non-resonant $\pi^+\pi^-$ as well as $\pi^+\pi^-\pi^0$ production. Total cross sections, angular distributions both of ω-mesons and protons were measured in the overall CMS as well as helicity and Jackson angle distributions in both the pp and ωp helicity and Jackson frames, respectively. In addition, the orientation of the ω-spin and invariant mass spectra were determined. All total cross sections obtained by integrating the various differential distributions agree within uncertainty, proving the consistency of our data evaluation.

The major results are as follows: We conclude from the angular distribution of the ω-meson that its production takes place dominantly in Ss and Sp final states for the lower energies, where only little room is left for Ps final states, and, additionally, type Sd final states for the highest energy. The production of ω-mesons via N^*-resonances was ruled out to be the major reaction mechanism. It is, however, conceivable that resonant ω-production via the broad subthreshold resonances S_{11} and D_{13} as well as resonances above threshold, P_{11} and P_{13}, may happen for particular initial states. However it probably plays a minor role among the various ω production mechanisms discussed in the literature. Invariant mass spectra for both the pp and pω subsystems are found to be compatible with phase space distributions underlining the minor importance of resonant ω-production. A dominant role of $^3P_1$ and $^1S_0$ initial partial waves for ω-production was concluded from the orientation of the ω-spin. Although we observe anisotropic Jackson angle distributions in the ωp-Jackson frame we argue that this is not an indication of a resonance but rather a kinematical effect reflecting the anisotropy of the ω angular distribution in the overall CMS. The helicity angle distribution in the ωp-helicity frame shows an anisotropy which, in addition to the orientation of the ω-spin, is probably the most sensitive observable to judge the validity of various theoretical descriptions of the production process.

References

1. V. Flaminio *et al.*, CERN-HERA 84-10 (1984)
2. F. Balestra *et al.* (DISTO collaboration), Phys. Rev. Lett. **81**, 4572 (1998).
3. F. Balestra *et al.* (DISTO collaboration), Phys. Rev. C **63** 024004 (2001).
4. F. Hibou *et al.*, Phys. Rev. Lett. **83** 492 (1999).
5. S. Barsov *et al.*, Eur. Phys. J. A **31**, 95 (2007).
6. S. Abd El-Samad *et al.* (COSY-TOF collaboration), Phys. Lett. B **522**, 16 (2001).
7. M. Abdel-Bary *et al.* (COSY-TOF collaboration), Phys. Lett. B **647**, 351 (2007).
8. R. Machleidt et al. Phys. Rep. 149, 1 (1987), see also: R. Machleidt, "The Meson Theory of Nuclear Forces and Nuclear Matter" in Relativistic Dynamics and Quark-Nuclear Physics: Proc. Los Alamos Workshop, p.71 (1986).
9. A. A. Sibirtsev, Nucl. Phys. A **604**, 455 (1996).
10. K. Nakayama *et al.*, Phys. Rev. C **57**, 1580 (1998).
11. K. Tsushima, K. Nakayama, Phys. Rev. C **68**, 034612 (2003).
12. K. Nakayama *et al.*, Phys. Lett. B **648**, 351 (2007).
13. C. Fuchs *et al.*, Phys. Rev. C **67**, 025202 (2003).
14. A. Faessler *et al.*, Phys. Rev. C **70**, 035211 (2004).
15. L. P. Kaptari, B. Kämpfer, Eur. Phys. J. A **23**, 291 (2004).
16. A. I. Titov *et al.*, Phys. Rev. C **65**, 065202 (2002).
17. M. Abdel-Bary *et al.* (COSY-TOF-collaboration), Phys. Lett. B **649**, 252 (2007).
18. M. Abdel-Bary *et al.* (COSY-TOF collaboration), Phys. Lett. B **662**, 14 (2008).
19. W. Ullrich for the COSY-TOF collaboration, IJMPA **24**, 454 (2009).
20. S. Abdel Samad *et al.*, Nucl. Instrum. Methods Phys. Res. A **556**, 20 (2006).
21. R. Bilger *et al.*, Phys. Lett. B **420**, 217 (1998).
22. M. Dahmen *et al.*, Nucl. Instruments Methods Phys. Res. A **348**, 97 (1994).
23. A. Böhm *et al.*, Nucl. Instruments Methods Phys. Res. A **443**, 238 (2000).
24. C. Amsler *et al.* (Particle Data Group), Physics Letters B **667**, 1 (2008).
25. M. Altmeier *et al.*, Eur. Phys. J. A **23**, 351-364 (2005).
26. S. Brand, PhD Thesis, Ruhr-Universität Bochum (1995).
27. U. Zielinsky, PhD Thesis, Ruhr-Universität Bochum (1999).
28. GENBOD, CERN Program Library Long Write-up W515 (1993).
29. L. Karsch, PhD Thesis, Technische Universität Dresden (2003).
30. M. Schulte-Wissermann, PhD Thesis, Technische Universität Dresden (2004).
31. C. Hanhart, Phys. Rep. **397**, 155-256 (2004) and private communications.
32. M. Post, U. Mosel, Nuclear Physics A **688**, 808–822 (2001).
33. J. M. Blatt, L. C. Biedenharn, Rev. Mod. Phys. **24**, 258 (1952).
34. K. Gottfried, J. D. Jackson, Nuovo Cimento **33**, 309 (1964)
35. A. I. Titov *et al.*, Phys. Rev. C **59**, 999 (1999).
36. M. P. Rekalo *et al.*, Z. Phys. A **357**, 133 (1997).
37. M. Hartmann *et al.*, Phys. Rev. Lett. **96**, 242301 (2006).
38. A. I. Titov, T.-S. H. Lee, Phys. Rev. C **67**, 065205 (2003).
39. E. Byckling, K. Kajantie, Particle Kinematics, John Wiley & Sons, 1973, ISBN 0 471 12885 6
40. A. A. Sibirtsev *et al.*, Eur.Phys.J. A **27** 269 (2006).

Appendix

Table 7. Differential cross sections in μb/sr of the angular distributions. The central value of a cosine interval of 0.2 or 0.1 is listed.

	$\cos\theta$	$\frac{d\sigma}{d\Omega}(\theta_\omega)$	$\frac{d\sigma}{d\Omega}(\theta_p)$	$\frac{d\sigma}{d\Omega}(\theta_{\omega p}^{Rpp})$	$\frac{d\sigma}{d\Omega}(\cos\theta_{p\omega}^{R\omega p})$	$\frac{d\sigma}{d\Omega}(\cos\theta_{bp}^{Rpp})$	$\frac{d\sigma}{d\Omega}(\cos\theta_{b\omega}^{R\omega p})$
$\varepsilon = 92$ MeV	-0.9		0.69 ± 0.23	0.72 ± 0.15	0.83 ± 0.18	0.73 ± 0.22	0.75 ± 0.11
	-0.7		0.84 ± 0.15	0.69 ± 0.11	0.76 ± 0.12	0.64 ± 0.14	0.76 ± 0.10
	-0.5		0.50 ± 0.12	0.69 ± 0.13	0.74 ± 0.11	0.78 ± 0.12	0.57 ± 0.10
	-0.3		0.73 ± 0.15	0.73 ± 0.13	0.85 ± 0.15	0.80 ± 0.08	0.70 ± 0.10
	-0.1		0.70 ± 0.13	0.69 ± 0.12	0.50 ± 0.13	0.75 ± 0.08	0.65 ± 0.08
	0.1	0.72 ± 0.11	0.77 ± 0.10	0.69 ± 0.12	0.72 ± 0.14	0.75 ± 0.08	0.72 ± 0.09
	0.3	0.56 ± 0.21	0.42 ± 0.13	0.73 ± 0.13	0.79 ± 0.14	0.80 ± 0.08	0.69 ± 0.08
	0.5	0.54 ± 0.19	0.47 ± 0.24	0.69 ± 0.13	0.80 ± 0.15	0.78 ± 0.12	0.63 ± 0.09
	0.7	0.86 ± 0.21	0.79 ± 0.24	0.69 ± 0.11	0.62 ± 0.12	0.64 ± 0.14	0.59 ± 0.11
	0.9	0.88 ± 0.24	0.89 ± 0.41	0.72 ± 0.15	0.73 ± 0.16	0.73 ± 0.22	0.83 ± 0.11
$\varepsilon = 128$ MeV	-0.95		1.03 ± 0.22	1.08 ± 0.20	0.95 ± 0.11	0.99 ± 0.25	1.15 ± 0.21
	-0.85		1.09 ± 0.06	0.88 ± 0.15	0.84 ± 0.13	1.02 ± 0.11	1.22 ± 0.12
	-0.75		1.06 ± 0.10	0.96 ± 0.15	0.91 ± 0.14	1.08 ± 0.08	1.13 ± 0.10
	-0.65		1.00 ± 0.09	1.04 ± 0.12	0.84 ± 0.11	1.02 ± 0.06	1.02 ± 0.10
	-0.55		0.99 ± 0.08	0.99 ± 0.11	0.95 ± 0.11	1.04 ± 0.09	1.02 ± 0.08
	-0.45		0.99 ± 0.08	1.00 ± 0.13	1.00 ± 0.11	1.01 ± 0.08	0.97 ± 0.07
	-0.35		0.98 ± 0.08	0.94 ± 0.09	0.98 ± 0.10	0.98 ± 0.08	0.97 ± 0.05
	-0.25		0.91 ± 0.09	1.09 ± 0.05	1.00 ± 0.09	0.99 ± 0.07	0.90 ± 0.05
	-0.15		0.95 ± 0.07	1.04 ± 0.05	1.02 ± 0.11	0.96 ± 0.07	0.90 ± 0.04
	-0.05		0.97 ± 0.07	1.04 ± 0.10	1.10 ± 0.12	0.94 ± 0.07	0.82 ± 0.08
	0.05	0.77 ± 0.12	0.95 ± 0.11	1.04 ± 0.10	1.14 ± 0.11	0.94 ± 0.07	0.79 ± 0.05
	0.15	0.78 ± 0.11	0.97 ± 0.09	1.04 ± 0.05	1.11 ± 0.11	0.96 ± 0.07	0.80 ± 0.05
	0.25	0.82 ± 0.05	0.95 ± 0.09	1.09 ± 0.05	1.14 ± 0.12	0.99 ± 0.07	0.87 ± 0.05
	0.35	0.87 ± 0.09	1.01 ± 0.08	0.94 ± 0.09	1.15 ± 0.09	0.98 ± 0.08	0.87 ± 0.10
	0.45	0.91 ± 0.04	0.92 ± 0.11	1.00 ± 0.13	1.17 ± 0.09	1.01 ± 0.08	0.90 ± 0.08
	0.55	0.96 ± 0.09	1.00 ± 0.14	0.99 ± 0.11	1.05 ± 0.11	1.04 ± 0.09	0.94 ± 0.06
	0.65	1.06 ± 0.10	1.04 ± 0.14	1.04 ± 0.12	1.00 ± 0.11	1.02 ± 0.06	1.10 ± 0.10
	0.75	1.12 ± 0.12	1.06 ± 0.18	0.96 ± 0.15	1.00 ± 0.10	1.08 ± 0.08	1.12 ± 0.13
	0.85	1.34 ± 0.19	0.98 ± 0.36	0.88 ± 0.15	0.89 ± 0.10	1.02 ± 0.11	1.18 ± 0.13
	0.95	1.56 ± 0.22	1.02 ± 0.42	1.08 ± 0.20	0.90 ± 0.11	0.99 ± 0.25	1.31 ± 0.06
$\varepsilon = 173$ MeV	-0.95		2.46 ± 0.42	2.86 ± 0.37	3.14 ± 0.56	2.41 ± 0.57	2.47 ± 0.37
	-0.85		2.43 ± 0.45	2.28 ± 0.47	2.14 ± 0.44	2.51 ± 0.33	2.45 ± 0.36
	-0.75		1.89 ± 0.43	1.75 ± 0.38	2.26 ± 0.65	2.47 ± 0.33	2.25 ± 0.32
	-0.65		2.53 ± 0.41	2.13 ± 0.44	1.66 ± 0.35	2.07 ± 0.29	1.99 ± 0.36
	-0.55		2.33 ± 0.38	2.25 ± 0.51	2.15 ± 0.38	2.21 ± 0.32	2.13 ± 0.31
	-0.45		1.89 ± 0.35	2.04 ± 0.39	1.86 ± 0.54	2.25 ± 0.32	2.67 ± 0.33
	-0.35		2.08 ± 0.36	2.30 ± 0.43	2.49 ± 0.42	2.17 ± 0.23	2.10 ± 0.34
	-0.25		2.11 ± 0.34	2.10 ± 0.45	1.50 ± 0.51	1.56 ± 0.36	1.80 ± 0.24
	-0.15		1.98 ± 0.41	2.05 ± 0.41	2.20 ± 0.37	1.83 ± 0.32	1.72 ± 0.27
	-0.05		1.76 ± 0.37	1.61 ± 0.46	2.25 ± 0.38	2.13 ± 0.39	2.12 ± 0.27
	0.05	1.80 ± 0.53	2.16 ± 0.35	1.61 ± 0.46	2.12 ± 0.37	2.13 ± 0.39	1.30 ± 0.24
	0.15	2.37 ± 0.49	2.42 ± 0.49	2.05 ± 0.41	2.21 ± 0.37	1.83 ± 0.32	1.81 ± 0.31
	0.25	2.28 ± 0.39	2.23 ± 0.38	2.10 ± 0.45	2.31 ± 0.39	1.56 ± 0.36	1.64 ± 0.31
	0.35	1.96 ± 0.31	2.90 ± 0.51	2.30 ± 0.43	2.85 ± 0.41	2.17 ± 0.23	1.78 ± 0.24
	0.45	2.41 ± 0.40	1.78 ± 0.51	2.04 ± 0.39	2.34 ± 0.48	2.25 ± 0.32	2.08 ± 0.40
	0.55	1.87 ± 0.29	1.92 ± 0.50	2.25 ± 0.51	1.77 ± 0.44	2.21 ± 0.32	1.89 ± 0.29
	0.65	2.24 ± 0.35	2.00 ± 0.66	2.13 ± 0.44	1.82 ± 0.43	2.07 ± 0.29	2.37 ± 0.30
	0.75	2.27 ± 0.39	3.51 ± 0.81	1.75 ± 0.38	2.14 ± 0.40	2.47 ± 0.33	2.00 ± 0.38
	0.85	3.04 ± 0.36	2.47 ± 0.78	2.28 ± 0.47	2.27 ± 0.43	2.51 ± 0.33	2.37 ± 0.38
	0.95	4.04 ± 0.41	2.06 ± 1.24	2.86 ± 0.37	1.49 ± 0.43	2.41 ± 0.57	3.29 ± 0.33

Table 8. Differential cross sections in μb/sr for the orientation of the ω decay plane at the different excess energies. The central value of a cosine interval of 0.2 is listed.

$\cos\gamma$	$\varepsilon = 92$ MeV	$\varepsilon = 128$ MeV	$\varepsilon = 173$ MeV
0.1	0.58 ± 0.45	0.65 ± 0.09	2.21 ± 0.57
0.3	0.35 ± 0.17	0.76 ± 0.06	1.78 ± 0.48
0.5	0.87 ± 0.18	0.96 ± 0.04	2.13 ± 0.28
0.7	0.70 ± 0.15	1.04 ± 0.03	2.21 ± 0.45
0.9	0.94 ± 0.15	1.28 ± 0.03	2.85 ± 0.33

Table 9. Differential cross sections in μb/sr for the invariant mass of the ωp-system, statistical errors are given only. The central mass of an interval of 10 MeV/c^2 is listed.

$M_{\omega p}$ (MeV/c^2)	$\varepsilon = 92$ MeV	$\varepsilon = 128$ MeV	$\varepsilon = 173$ MeV
1715	0.16 ± 0.07	0.16 ± 0.01	0.30 ± 0.07
1725	0.45 ± 0.08	0.40 ± 0.01	0.54 ± 0.10
1735	0.91 ± 0.11	0.78 ± 0.02	1.21 ± 0.17
1745	1.18 ± 0.12	1.20 ± 0.02	1.58 ± 0.24
1755	1.28 ± 0.12	1.19 ± 0.02	1.34 ± 0.22
1765	1.17 ± 0.13	1.31 ± 0.02	1.97 ± 0.24
1775	1.26 ± 0.13	1.27 ± 0.02	1.65 ± 0.24
1785	1.37 ± 0.13	1.27 ± 0.02	2.52 ± 0.25
1795	1.24 ± 0.11	1.28 ± 0.02	2.07 ± 0.24
1805	0.78 ± 0.10	1.13 ± 0.02	1.89 ± 0.23
1815		1.25 ± 0.02	2.08 ± 0.23
1825		0.99 ± 0.02	1.67 ± 0.23
1835		0.64 ± 0.02	2.26 ± 0.23
1845		0.42 ± 0.02	2.11 ± 0.22
1855			1.74 ± 0.20
1865			1.81 ± 0.20
1875			1.49 ± 0.18
1885			0.86 ± 0.15

Table 10. Differential cross sections in μb/sr for the invariant mass of the pp-system, statistical errors are given only. The central mass of an interval of 10 MeV/c^2 is listed.

M_{pp} (MeV/c^2)	$\varepsilon = 92$ MeV	$\varepsilon = 128$ MeV	$\varepsilon = 173$ MeV
1882	0.95 ± 0.15	0.69 ± 0.02	1.27 ± 0.23
1892	1.05 ± 0.15	0.77 ± 0.02	1.29 ± 0.24
1902	1.29 ± 0.17	1.10 ± 0.03	0.83 ± 0.26
1912	1.20 ± 0.18	1.03 ± 0.03	1.07 ± 0.25
1922	1.32 ± 0.18	1.24 ± 0.03	1.73 ± 0.28
1932	1.44 ± 0.18	1.59 ± 0.03	2.77 ± 0.29
1942	0.94 ± 0.15	1.41 ± 0.03	1.99 ± 0.35
1952	1.25 ± 0.17	1.34 ± 0.03	2.40 ± 0.31
1962	0.41 ± 0.15	1.30 ± 0.03	2.48 ± 0.33
1972	0.01 ± 0.16	1.11 ± 0.03	1.70 ± 0.32
1982		0.97 ± 0.03	2.04 ± 0.31
1992		0.44 ± 0.02	2.60 ± 0.31
2002		0.23 ± 0.01	2.07 ± 0.32
2012			2.00 ± 0.33
2022			1.55 ± 0.30
2032			0.89 ± 0.26
2042			0.91 ± 0.25